Advanced Energy Materials

ADVANCED ENERGY MATERIALS
www.advenergymat.de

RESEARCH ARTICLE OPEN ACCESS

In Situ Measurement of Oxygen Vacancy Dynamics and Surface Exchange Reactions in Oxide Electrode under Solid Electrochemical Cell Operating Conditions

Taeyun Kim[1] | Jinsil Lee[1] | Hee Jung Park[2,3] | Ji Haeng Yu[4] | José M. Serra[5] | Jong Hoon Joo[1,6]

[1]Department of Environment and Energy Engineering, Gwangju Institute of Science and Technology (GIST), Gwangju, Republic of Korea | [2]Department of Materials Science and Engineering, Dankook University, Cheonan, Republic of Korea | [3]Hydrogen Research Center, Dankook University, Cheonan, Republic of Korea | [4]High Temperature Energy Conversion Laboratory, Korea Institute of Energy Research (KIER), Daejeon, Republic of Korea | [5]Instituto de Tecnología Química (Universitat Politècnica de Valèencia – Consejo Superior de Investigaciones Científicas), Valencia, Spain | [6]Research Center for Innovative Energy and Carbon Optimized Synthesis for Chemicals (Inn-ECOSysChem), Gwangju Institute of Science and Technology (GIST), Gwangju, Republic of Korea

Correspondence: Jong Hoon Joo (jhjoo@gist.ac.kr)

Received: 3 December 2025 | **Revised:** 29 January 2026 | **Accepted:** 4 February 2026

Keywords: oxygen vacancy | perovskite electrodes | solid oxide electrochemical cells (SOCs) | surface exchange coefficient

ABSTRACT

Solid oxide electrochemical cells (SOCs) employ mixed ionic–electronic conducting (MIEC) perovskite electrodes, where electrochemical performance is dictated by the oxygen surface exchange coefficient (k) and the concentration of oxygen vacancies (δ). Conventional methods evaluate k and δ separately and under conditions that do not reflect their coupled behavior during operation, offering only a partial picture of the underlying processes. Here we report an in situ methodology that simultaneously resolves k and δ under realistic SOC operating conditions, using a dense bulk electrode integrated with a solid electrolyte. An applied overpotential induces an abrupt drop in the oxygen chemical potential gradient, enabling direct analysis of defect chemistry and surface reaction kinetics. The extracted values are consistent with those obtained from established characterization methods, validating the accuracy of the approach. Beyond fundamental characterization, the platform captures dynamic evolutions in defect chemistry and reaction kinetics, providing mechanistic insights into electrode degradation.

1 | Introduction

Solid oxide electrochemical cells (SOCs) operate at high temperatures, enabling efficient conversion of fuels into electricity (as in solid oxide fuel cells, SOFCs), or, conversely, the use of electricity to convert substances such as water or CO_2 into valuable fuels and chemicals (as in solid oxide electrolysis cells, SOECs) [1–9]. However, the elevated operating temperatures accelerate long-term performance degradation through a combination of interfacial chemical interdiffusion, thermomechanical stress-induced cracking, catalytic degradation, phase decomposition, and electrode delamination [10–19]. Additionally, the harsh thermal environment limits the selection of durable materials for components such as interconnects, electrolytes, and electrodes, presenting challenges for large-scale commercialization [5, 11, 12, 20]. Among these components, the air electrode plays a critical role in determining the overall electrochemical performance of SOCs [10, 21–25]. Consequently, extensive efforts have been devoted to the development of intermediate-temperature SOCs (IT-SOCs), which typically use perovskite-type oxides exhibiting high mixed ionic and electronic conductivity (MIEC) [26–29]. While various MIEC materials such as $Ba_{1-x}Sr_xCo_{1-y}Fe_yO_{3-\delta}$ (BSCF) and $Sm_{1-x}Sr_xCoO_{3-\delta}$ (SSC) have been actively explored as air electrode candidates, $La_{1-x}Sr_xCo_{1-y}Fe_yO_{3-\delta}$ (LSCF) is widely used owing to its favorable balance of electrochemical activity, thermochemical stability, and compatibility with conventional

electrolytes [30]. Consequently, LSCF-based materials are experiencing widespread adoption in both academic and commercial SOC systems [31–36]. In IT-SOCs, the reduced operating temperature significantly slows the oxygen exchange kinetics at the air electrode, making it the rate-determining step (RDS) of the electrode reaction [37–39]. Thus, to achieve high performance, both the bulk oxygen diffusion and surface exchange kinetics of the air electrode material must be optimized [40]. Bulk diffusion is closely associated with oxygen ionic conductivity, which is strongly influenced by the concentration of oxygen vacancies (δ) [41, 42]. Surface exchange kinetics govern how efficiently oxygen molecules are incorporated during the oxygen reduction reaction (ORR) and released during the oxygen evolution reaction (OER) at the electrode surface [40, 43]. Therefore, intrinsic material properties such as oxygen vacancy concentration (δ) and surface exchange coefficient (k) are critical parameters that directly affect the performance of air electrodes with a given microstructure [44–48]. The δ values of electrode materials are typically determined using techniques such as thermogravimetry analysis (TGA) or coulometric titration based on chemical reactions [49–56]. Additionally, k represents a critical parameter for elucidating electrochemical reaction kinetics and can be quantified via electrical (k^q), tracer (k^*), and chemical (k_{chem}) surface exchange coefficients. Experimental approaches such as electrical conductivity relaxation (ECR) and oxygen isotope exchange are commonly used for determining k values [57–64].

However, the conventional methods for determining k and δ are typically conducted under conditions that deviate from the actual operating environment of SOCs. Consequently, the obtained measurements primarily reflect the intrinsic properties of the materials, rather than their electrochemical behavior in a cell-integrated configuration involving significant interactions with the electrolyte and electrode interfaces. This aspect limits the direct applicability of the measured values to real operating cell systems. To overcome this issue, various efforts have been made to evaluate k and δ under realistic operating conditions using electrochemical impedance spectroscopy (EIS) on thin-film model electrodes [65–69]. However, these thin-film electrodes are typically fabricated by pulsed laser deposition (PLD), and owing to factors such as lattice strain, nanocrystalline effects, and accelerated cation diffusion in thin films compared with bulk materials, discrepancies have been observed in the oxygen vacancy behavior and thermodynamic properties of electronic defects [70, 71]. These differences render it challenging to extrapolate thin-film measurements to bulk electrode behavior in practical SOC systems. Although the fundamental properties of electrode materials, such as k and δ, have been extensively investigated, their temporal evolution under realistic operating conditions remains poorly understood. To address this limitation and accurately capture the dynamic changes in these properties, in situ characterization is crucial for elucidating degradation mechanisms, thereby promoting SOC commercialization.

In this study, we present a novel methodology for directly and simultaneously quantifying k and δ under realistic electrochemical operating conditions. In a dense bulk electrode architecture integrated with a solid electrolyte, the application of an overpotential induces an oxygen chemical potential gradient. This configuration enables in situ determination of both bulk defect chemistry and surface exchange kinetics, along with the estimation of hole polaron concentrations, thereby providing a unified framework to probe the electrochemical behavior of electrode materials under operating conditions. Beyond merely validating intrinsic material properties, the present approach enables a more comprehensive understanding of overall electrode behavior. The significance of this methodology lies in its capability to simultaneously quantify the surface exchange coefficient (k), the oxygen vacancy concentration (δ), and the hole concentration within a single electrochemical framework. By concurrently tracking the evolution of these parameters, this approach allows for a direct correlation between defect chemistry and electrochemical kinetics. Consequently, the methodology serves as a powerful diagnostic tool for probing complex degradation mechanisms, thereby providing deeper insight into electrode durability. The validity of the proposed method is demonstrated using $La_{1-x}Sr_xFeO_{3-\delta}$ (LSF), one of the most representative perovskite-type materials for SOC electrodes, yielding values for k and δ in close agreement with those reported in the literature. This confirms the reliability of our approach and establishes a foundation for the development of advanced in situ characterization techniques.

2 | Results and Discussion

2.1 | Fabrication and Electrochemical Analysis of Dense Bulk Electrode

LSF is one of the most widely used air electrode materials in SOCs, owing to its high electronic conductivity, reasonable oxygen ion transport, and well-established defect chemistry [39, 51, 72, 73]. Its extensive use in both fundamental research and practical applications makes it an ideal model system for investigating oxygen surface exchange kinetics and defect evolution. Moreover, LSF exhibits representative behavior for a broad class of perovskite-type MIEC electrodes such as LSCF and BSCF, facilitating the comparison and validation of key electrochemical parameters across systems. As shown in Figure 1a, the oxygen exchange reaction involves multiple elementary steps, including adsorption, dissociation, incorporation, and diffusion of oxygen species [74, 75]. Among these, the surface exchange reaction is widely regarded as the RDS under typical cathodic conditions [76, 77]. Therefore, k, which quantifies the rate of oxygen exchange at the electrode surface, and δ, which governs the availability of ionic transport pathways and active sites, are considered key parameters for evaluating and optimizing electrode performance. In general, k is determined using ECR or secondary ion mass spectrometry (SIMS), while δ is extracted from TGA or coulometric titration. However, these analyses are typically not conducted under realistic SOC operating conditions, where the material is integrated with an electrolyte. To address these limitations, efforts have been made to develop experimental systems that more accurately simulate the actual operating conditions of SOCs. Notably, conventional porous electrodes present inherent challenges in decoupling intrinsic surface reaction kinetics owing to their complex architecture, which convolves gas-phase diffusion, bulk transport, and surface exchange reaction processes, obscuring the ability to isolate and quantify surface-specific exchange behavior (Figure 1b) [78]. As a solution, dense electrode structures have been used to eliminate the influence of gas-phase diffusion and the ambiguity associated with defining the exact surface area. In such configurations, the oxygen exchange process

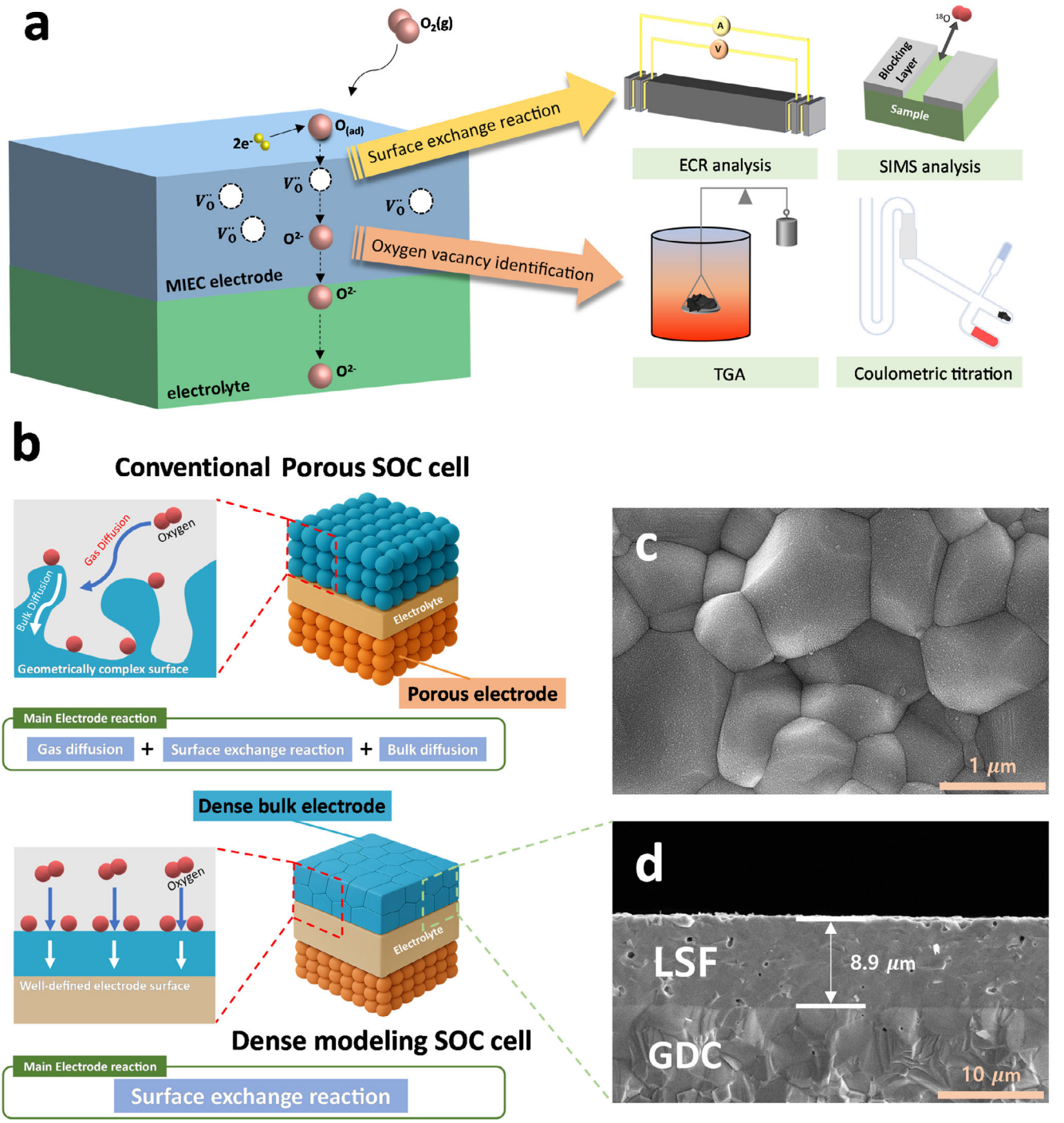

FIGURE 1 | Schematic and surface characterization of LSF dense bulk electrode. a) Illustration of oxygen incorporation reaction and methods for evaluating surface exchange reaction and oxygen vacancies. b) Schematic of dense bulk electrode system. c) Top-view scanning electron microscope (SEM) image of LSF64 electrode. d) Cross-sectional SEM image of LSF64 electrode.

can be analyzed without interference from porous architecture or tortuosity effects. Furthermore, to ensure that the system operates within a surface exchange-limited regime, the electrode thickness (L) was maintained significantly smaller than the characteristic thickness ($L_c = D/k$), where D and k are the oxygen diffusion and surface exchange coefficients, respectively. When the electrode thickness is substantially smaller than L_c, typically by several orders of magnitude, oxygen transport is dominated by surface exchange kinetics rather than bulk diffusion. Under these conditions, the contribution from bulk diffusion can be reasonably neglected, ensuring that the measured kinetics accurately reflect surface-limited processes. Although dense thin films fabricated by PLD have been used to accurately simulate practical systems, the δ values derived from these model systems often deviate from bulk data, indicating discrepancies between experimental configurations and actual device environments. Furthermore, k and δ are typically evaluated independently, overlooking their coupled evolution under SOC operating conditions. These

factors render it challenging to comprehensively understand the interrelationship between these two critical factors. To overcome these limitations and enable the simultaneous, in situ quantification of k and δ under realistic electrochemical conditions, we employ a dense bulk LSF electrode co-sintered directly onto a $Gd_{0.1}Ce_{0.9}O_{1.95}$ (GDC) electrolyte. To implement this approach, an electrochemical cell is constructed using an asymmetric electrode configuration, consisting of a dense LSF working electrode (WE) and a porous LSCF counter electrode (CE).

As shown in Figure 1c,d, the LSF electrode exhibits a well-sintered and dense microstructure, which is essential for ensuring a geometrically defined surface area. According to reference data for the $La_{0.6}Sr_{0.4}FeO_{3-\delta}$ (LSF64) at 725°C, D_{chem} and k_{chem} are ~3 × 10^{-6} cm^2/s and ~3 × 10^{-5} cm/s, respectively [79, 80]. Based on these values, L_c is calculated to be ~10^3 µm. Since our dense bulk electrode has a thickness of approximately 8.9 µm, which is more than two orders of magnitude smaller than L_c, the oxygen transport is theoretically dominated by surface exchange kinetics. Furthermore, despite the formation of a dense microstructure via co-sintering of the LSF electrode and GDC electrolyte, distinct LSF and GDC phases are observed in the X-ray diffraction (XRD) patterns (Figure S1b), with no detectable secondary phases resulting from interfacial reactions. To further investigate the chemical stability of the co-sintered interface, cross-sectional scanning electron microscopy (SEM) and energy dispersive X-ray (EDX) mapping were performed (Figure S1c). As confirmed by the EDX mapping results, interdiffusion is observed at the LSF/GDC interface, with an interdiffusion zone of approximately 1 µm. However, as will be discussed in the following electrochemical impedance spectroscopy (EIS) analysis, the electrode/electrolyte interfacial reaction is clearly distinguished from the surface exchange reaction. Consequently, despite the presence of minor interdiffusion, its effect is confined to the interfacial component and remains decoupled in the EIS analysis, such that it does not influence the extracted k value. Therefore, the impact of interdiffusion on the determined k and δ values can be considered negligible. As discussed in detail later, the measured resistance of the symmetric porous LSCF electrode is approximately 0.72 Ω (Figure S2). Accordingly, the resistance attributed to a single porous counter electrode (~0.36 Ω) accounts for only 1%–2% of the total cell resistance. This minimal contribution indicates that the CE has a negligible impact on the overall impedance response. Consequently, the system enables reliable characterization of the dense LSF working electrode, effectively excluding interference from the counter electrode. Furthermore, as the electrode is directly integrated with the electrolyte, the system closely resembles the actual configuration of SOCs, enabling the investigation of electrode processes under realistic conditions [10, 16, 17, 23, 81].

Figure 2a shows a representative Nyquist plot of the LSF64 dense bulk electrode cell measured at 700°C under open circuit voltage (OCV) conditions in ambient air. The equivalent circuit shown in Figure 2a is used to clarify the impedance characteristics. Our previous research demonstrated that this circuit can be represented by one resistance element in series with two parallel R–CPE components (where CPE denotes a constant phase element) [10, 16, 17, 23, 81]. The impedance pattern can be divided into three regions: the intersection with the x-axis in the high-frequency region, corresponding to the electrolyte resistance (R_b); the first arc in the mid-frequency region, corresponding to the electrode/electrolyte interfacial resistance (R_i) associated with oxygen ion transfer across the interface; and the second arc in the low-frequency region, corresponding to the electrode surface exchange resistance (R_s). According to the Nyquist plot, R_b is approximately 4.27 Ω. Considering the geometric factor based on the GDC electrolyte thickness of 440 µm as verified by cross-sectional SEM (Figure S3), the calculated ionic conductivity is approximately 2.5 × 10^{-2} S/cm. This result is in good agreement with the literature value (2.7 × 10^{-2} S/cm at 700°C), supporting the reliability of the electrochemical measurements [82, 83].

Figure 2b presents the impedance spectra as a function of oxygen partial pressure (P_{O_2}) ranging from 2.1 × 10^{-4} to 1 atm at 700°C. Among the fitted parameters, R_s exhibits a pronounced variation with changes in P_{O_2}, while R_b and R_i remain relatively constant. This indicates that the surface oxygen exchange reaction is highly sensitive to P_{O_2} and thus governs electrode performance under these conditions [84, 85]. Identifying the RDS in the multistep process of oxygen surface reaction is essential for elucidating the electrochemical behavior of the electrode and improving the overall efficiency of SOCs. According to established defect-chemical models, the oxygen surface exchange reaction proceeds through a sequence of elementary steps involving molecular oxygen adsorption, dissociation, electron transfer, and incorporation of oxygen ions into the lattice. The dependence of the surface exchange resistance on oxygen partial pressure provides important insight into the underlying reaction mechanism. Analyzing the dependence of R_s on P_{O_2} represents a practical method for identifying the RDS, based on the relationship $R_s \propto P_{O_2}^{-m}$, where m is an integer. As shown in Figure 2c, a slope of approximately 0.25 is observed. Such quarter-order dependence has been widely reported for MIEC electrodes, including LSF-based perovskites, and is commonly associated with charge transfer-limited surface exchange kinetics [23, 81]. Nevertheless, it should be noted that slope-based analysis relies on simplified defect-chemical descriptions and may not fully capture additional surface complexities, such as variations in surface potential, changes in intermediate coverage, or parallel reaction pathways. Within these recognized limitations, the excellent agreement between the experimentally observed slope and well-established mechanistic frameworks supports the assignment of the rate-determining step to charge transfer in the present study. However, this interpretation may not be definitive, as multiple overlapping processes and experimental uncertainties can hinder the accurate identification of the RDS. Therefore, rigorous characterization and comprehensive analysis are essential for resolving these uncertainties and enhancing the understanding of the underlying electrochemical mechanisms.

Figure 2d further highlights the effectiveness of the dense bulk electrode system. The activation energies are consistent with reported values [86, 87], supporting the reliability of the experimental setup. Notably, the activation energy associated with R_s is significantly higher than that of R_b and R_i, confirming that surface reaction kinetics are the principal limiting factor in the performance of dense electrode.

In this study, the use of a CPE allows more accurate fitting of the impedance data and enables the extraction of meaningful

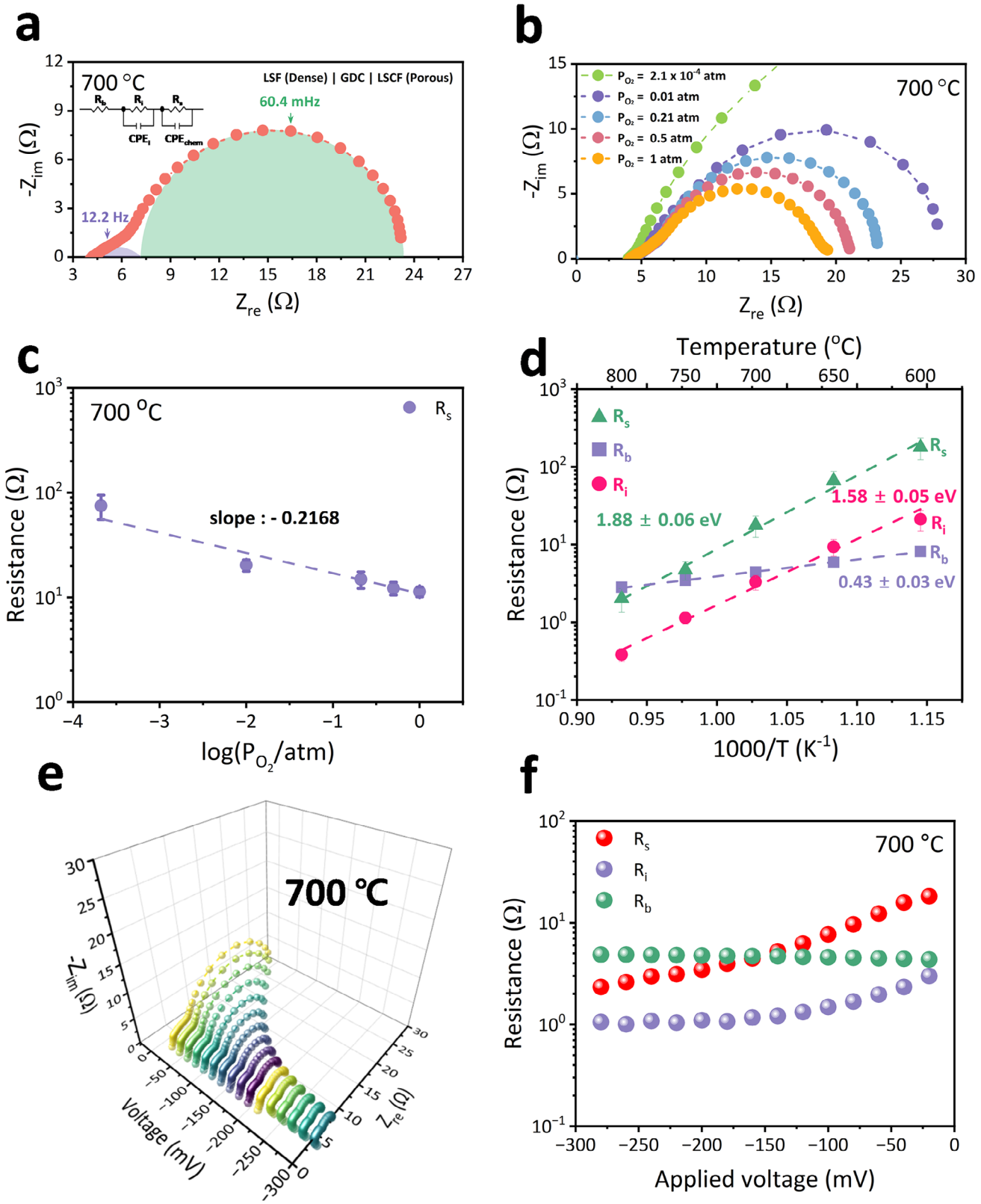

FIGURE 2 | Electrochemical characteristics of LSF64 dense bulk electrode. a) Nyquist plot at 700°C under open circuit voltage condition. b) Impedance spectra at various oxygen partial pressures at 700°C. c) Dependence of surface exchange resistance (R_s), electrolyte resistance (R_b), and electrode/electrolyte interface resistance (R_i) on oxygen partial pressure. d) Temperature dependence of e) Nyquist plots under various cathodic bias conditions. f) Variations in resistance factors (R_s, R_b and R_i) with cathodic bias.

parameters such as the area-specific chemical capacitance (C_δ) associated with surface reaction processes. The dominant capacitive feature observed in this regime corresponds to the C_δ, which arises from variations in chemical species in the electrode bulk and is influenced by the surface reaction. Consequently, the low-frequency arc is represented by a parallel combination of R_s and C_δ [70, 88, 89]. The use of a geometrically well-defined electrode structure, which emphasizes the contribution of R_s and allows precise quantification of the active surface area, facilitates the reliable determination of the surface exchange coefficient (k^q) from the impedance spectra [23, 81, 90]. Specifically, k^q can be calculated as

$$k^q = \frac{k_B T}{4e^2 ASR c_O} \tag{1}$$

where k_B is the Boltzmann constant, T is the absolute temperature, e is the elementary charge, ASR is the area specific resistance, and c_O is the total concentration of lattice oxygen. This approach offers a direct relationship between impedance-derived surface resistance and the oxygen exchange kinetics at the electrode surface. While R_s provides insight into the kinetics of oxygen exchange at the electrode surface, the capacitive response offers complementary information regarding the chemical storage behavior within the electrode bulk. Notably, C_δ quantitatively represents the extent to which a material can accommodate or release charged species (e.g., oxygen vacancies or electron holes) in response to changes in chemical potential. In other words, it reflects the sensitivity of the defect concentration in the electrode to variations in the local oxygen chemical potential, which may be induced by external bias or changes in ambient conditions.

In general, for MIEC oxides, C_δ of the electrode layer is defined as

$$C_\delta = -\frac{4F^2 L}{V_m} \frac{d\delta}{d\mu_{O,WE}} \tag{2}$$

where F is the Faraday constant, V_m is the molar volume of the electrode material, and $\mu_{O,WE}$ is the oxygen chemical potential at the WE [70, 71].

According to Equation 2, the electrode chemical capacitance can be described as a function of μ_O. Thus, two key parameters k and δ can be derived from impedance spectroscopy, offering a pathway to correlate electrochemical performance with the thermodynamics (defect concentration) and kinetics of charge carriers. A detailed discussion of the extraction and interpretation of these parameters is presented in the next section.

According to the relationship between C_δ and δ, δ can be quantified from the measured C_δ. To systematically probe the dependence of δ on P_{O_2}, a cathodic overpotential is applied to the electrode, effectively decreasing the local P_{O_2} throughout the electrode bulk. This electrochemical approach allows for controlled modulation of defect chemistry under equilibrium conditions, enabling direct assessment of oxygen vacancy formation as a function of the electrochemical driving force. Applying a cathodic bias effectively lowers μ_O within the dense bulk electrode, promoting the formation of oxygen vacancies throughout the electrode interior. This modulation of the chemical potential is essential for quantitatively analyzing defect chemistry, particularly δ. This surface-limited behavior leads to a pronounced dependence of the impedance response on the applied cathodic bias, as illustrated in Figure 2e and Figure S4, which present the impedance spectra as a function of applied cathodic bias. As the cathodic bias increases, the oxygen incorporation reaction at the electrode surface becomes more thermodynamically favorable, effectively activating the surface reaction process. Consequently, R_s decreases, consistent with enhanced surface reaction kinetics under cathodic bias. A similar trend in bias dependence is observed not only for LSF64 but also for $La_{0.8}Sr_{0.2}FeO_{3-\delta}$ (LSF82) in Figure S5, indicating that this behavior is largely universal and not limited to a specific composition. Further impedance analysis based on the equivalent circuit is provided in Figure 2f, which quantitatively compares the evolution of individual resistance components with varying cathodic bias. While both surface and interfacial reaction processes improve with increasing applied potential, the reduction in R_s is significantly more pronounced than that of R_i. This trend, further corroborated by the Bode magnitude and phase angle plot as shown in Figure S6, demonstrates that R_s remains the dominant resistive component across the entire bias range. In particular, the marked decrease in R_s is attributed to the enhanced activation of the oxygen incorporation reaction at the electrode surface owing to cathodic polarization. These findings indicate that even under polarized conditions, the overall electrode kinetics are effectively governed by the surface exchange process rather than interfacial or bulk transport. Overall, the dense bulk electrode system, combined with impedance analysis, provides a reliable platform for elucidating oxygen surface reaction kinetics and defect dynamics in MIEC oxide electrodes.

2.2 | Estimation of Oxygen Vacancy using Chemical Capacitance

Departing from conventional SOC configurations that rely on differences in P_{O_2} between the cathode and anode, this work adopts an electrochemical approach to modulate the μ_O within a dense bulk electrode by applying an external cathodic bias under uniform gas conditions. Figure 3a,b schematically illustrates the variation in μ_O profiles within the dense bulk electrode system under different electrical conditions. Under OCV conditions, the electrode remains in thermodynamic equilibrium with ambient oxygen, resulting in a constant μ_O profile across the electrode. In contrast, when a cathodic bias is applied to the dense electrode, μ_O at the WE decreases, thermodynamically driving oxygen incorporation into the lattice. Furthermore, owing to the dense structure of the electrode and its thickness, which is significantly smaller than L_c, the overall rate of oxygen incorporation is governed predominantly by surface exchange kinetics rather than by the bulk diffusion of oxygen ions [10, 23, 81]. Under these surface-limited conditions, the overpotential applied across the electrode is primarily consumed at the electrode surface, where the ORR occurs. Consequently, the μ_O within the electrode bulk remains uniform but drops in proportion to the applied cathodic bias. This leads to a substantial and uniform decrease in μ_O throughout the electrode upon polarization, enabling spatially homogeneous modulation of

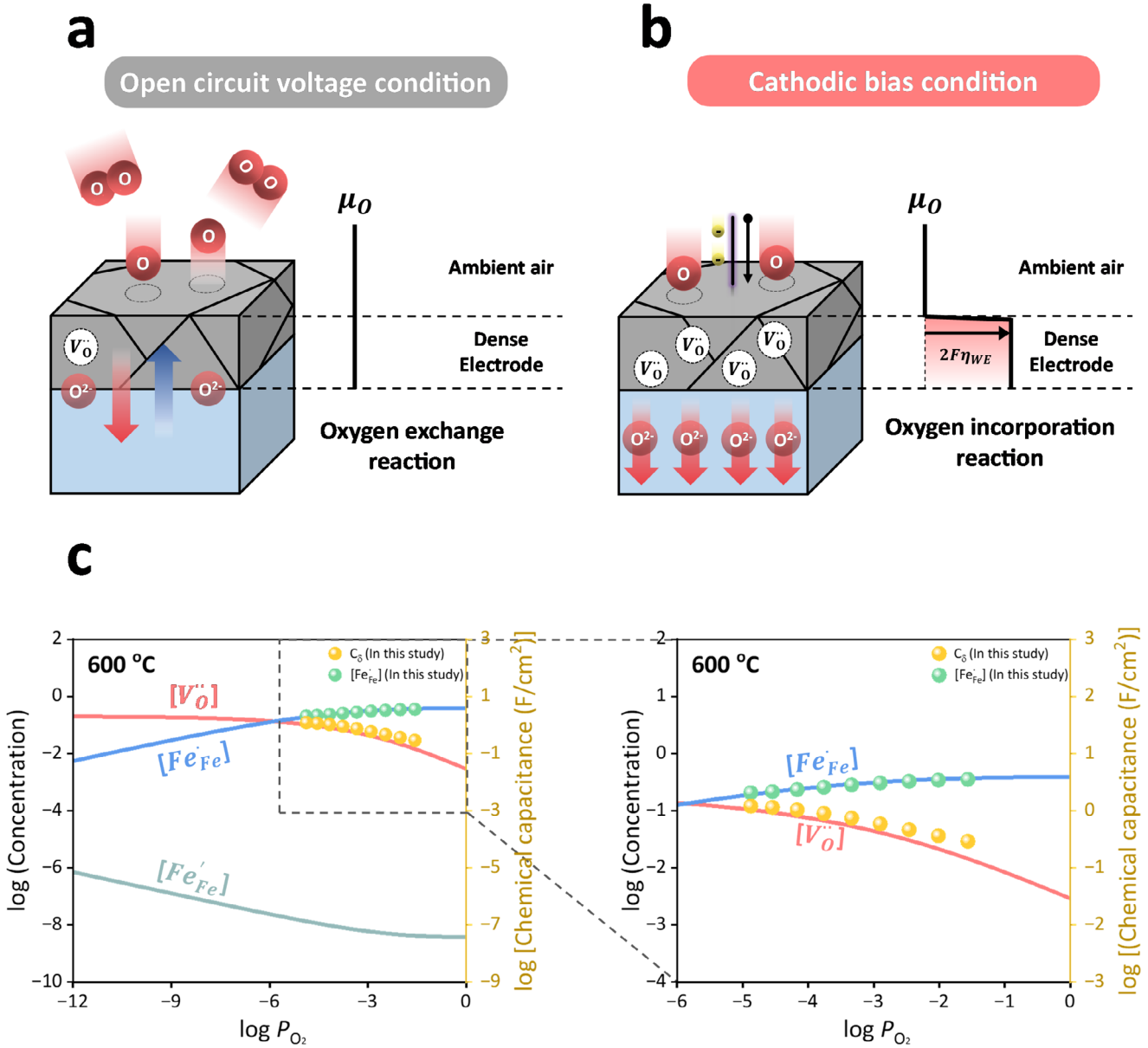

FIGURE 3 | Conceptual depiction of experimental data. a) Schematic image of LSF dense bulk electrode at open circuit voltage condition and b) cathodic bias condition. c) Brouwer diagram of LSF64 at 600°C (Solid circle: data from this study, Solid line: reference data of the concentration variation as a function of oxygen partial pressure [51]).

defect concentrations such as oxygen vacancies. This uniformity facilitates direct correlation between the applied voltage and the corresponding shift in μ_O, providing a reliable framework for quantifying bulk defect responses to electrochemical polarization.

This system design is particularly advantageous for impedance-based measurements, as it maximizes sensitivity to bulk defect responses while minimizing the influence of geometrical and microstructural complexities. The analytical expression describing the relationship between applied voltage and μ_O, along with its thermodynamic interpretation, is detailed in Figure S7 and Supporting information Section S1.

To further understand how the applied potential affects defect chemistry, it is essential to relate μ_O to the thermodynamic properties of LSF. Based on defect equilibrium and configurational entropy considerations, the following relationship can be established [70]:

$$\mu_O - \mu_O^\circ = h_O - h_O^\circ - T\left(s_O - s_O^\circ\right) = \Delta G_{ox}^\circ - RTln\frac{\delta}{(3-\delta)} \quad (3)$$

where h_O is the partial molar enthalpy, s_O is the partial molar entropy, ΔG_{ox}° is the standard Gibbs free energy change for the oxygen incorporation reaction, and R is the gas constant. The full derivation of Equation 3, including the assumptions and thermodynamic background, is provided in Supporting information Section S2 and S3. Equation 3 quantitatively describes the thermodynamic relationship between μ_O and δ, capturing the equilibrium condition for oxygen vacancy formation in the perovskite lattice. In addition, because μ_O is fundamentally related to

P_{O_2} through $\mu_O = \mu_O^\circ + \frac{1}{2}RT\ln P_{O_2}$, a further thermodynamic link between δ and P_{O_2} can be established (Supporting information Section S2). This relationship describes how δ varies with P_{O_2} under equilibrium conditions.

Combining Equations 2 and 3, the following analytical expression can be obtained:

$$C_\delta = \frac{4F^2L}{V_m} \cdot \frac{\delta(3-\delta)}{3RT} \tag{4}$$

This expression reveals a direct quantitative relationship between the experimentally measured C_δ and δ in bulk LSF. The electrode thickness is designed to be smaller than the characteristic thickness, allowing the assumption of a uniform distribution of oxygen vacancies throughout the electrode in the estimation of C_δ. Notably, this model is particularly applicable in the relatively oxidizing region ($\delta < x/2$), which corresponds to the practical operating conditions of SOC air electrode materials (Figure 3c). Under these conditions, electronic defect concentrations remain nearly constant [91], enabling simplification of entropy terms and yielding a predictable $C_\delta - \delta$ relationship.

Taken together, this approach demonstrates that impedance-derived C_δ can serve as a robust diagnostic tool for estimating δ for perovskite oxides. The consistency of this method with the defect chemistry of LSF, and by extension, with similar MIEC materials, validates its effectiveness and practical applicability under realistic operating conditions.

To quantitatively validate the relationship between C_δ and δ, C_δ is analyzed as a function of P_{O_2}. This analysis enables a direct correlation between defect chemistry and the electrochemical response of the dense LSF electrode under varying oxygen environments. The solid lines in Figure 4a–c represent the calculated C_δ plots for LSF as a function of P_{O_2}, derived using Equation 3 and thermodynamic parameters obtained from the literature [51]. In particular, the equilibrium constants required for the δ–P_{O_2} relationship are obtained from TGA under equilibrium conditions, as detailed in Supporting information Section S2. These plots serve as a reference based on bulk thermodynamic behavior, enabling a direct comparison with the experimentally measured capacitance of the present dense bulk electrode samples. Experimental data points (solid circles) were obtained from impedance spectroscopy under controlled cathodic bias, where the local oxygen partial pressure at the WE is related to the ambient oxygen partial pressure by

$$P_{O_2}^{WE} = P_{O_2}^{at} \cdot \exp\left(\frac{4F\eta_{WE}}{RT}\right) \tag{5}$$

where $P_{O_2}^{WE}$ and $P_{O_2}^{at}$ is the equivalent oxygen partial pressure of WE and the ambient atmosphere, respectively, and η_{WE} is the applied overpotential to WE.

For compositions with $x = 0.2$ and 0.4, the experimental C_δ shows strong consistency with the calculated trends, validating the reliability of the dense electrode configuration and measurement approach. Using Equation 4, δ can be extracted from the measured C_δ as

$$\delta = \frac{3}{2} - \sqrt{\frac{9}{4} - \frac{3C_\delta V_m RT}{4F^2L}} \tag{6}$$

As shown in Figure 4d–f, the experimentally determined oxygen vacancy concentrations exhibit good agreement with previously reported reference values and calculated results [92–94]. Notably, in Figure 4d, this level of agreement contrasts with previous reports obtained using thin-film model electrodes [71], where significant deviations from bulk δ–P_{O_2} behavior were often observed owing to strain effects [70, 71]. These results highlight a distinct advantage of the dense bulk electrode system: it closely represents bulk-like defect chemistry and enables accurate, operando quantification of key parameters such as δ. Consequently, impedance spectroscopy combined with dense electrode platforms provides a robust, dynamic, and non-destructive method for characterizing defect equilibria under practical SOC operating conditions.

In electrode reactions of MIEC oxides, not only oxygen vacancies, but also electronic defects play a critical role, with high performance depending on optimizing both electronic conductivity and oxygen vacancy concentrations, both of which can be quantitatively assessed using a dense bulk electrode system to better understand defect equilibria under operating conditions. Under relatively oxidizing conditions, LSF exhibits p-type conductivity; therefore, $[Fe'_{Fe}]$ can be considered negligible. As shown in Figure 3c, this allows the charge neutrality condition to be simplified to $x \approx [Fe^{\cdot}_{Fe}] + 2\delta$. This implies that, through impedance spectroscopy, $[Fe^{\cdot}_{Fe}]$ can be indirectly estimated from C_δ. This calculation is based on the direct coupling between the oxygen vacancy concentration and the hole concentration, as defined by the standard defect chemistry for LSF. As shown in Figure 5a–c, $[Fe^{\cdot}_{Fe}]$ values derived from impedance measurements exhibit good agreement with values reported in the literature [51]. The close match with reference bulk data confirms that the chosen analytical approach accurately represents the electronic state of the electrode. In LSF systems, Sr doping induces charge compensation primarily via the generation of $[Fe^{\cdot}_{Fe}]$ and δ. According to Figure 5d, at $x = 0.2$ and 600°C, $[Fe^{\cdot}_{Fe}]$ is approximately two orders of magnitude greater than the δ, indicating hole-dominated compensation. However, at $x = 0.4$, this ratio decreases to one order of magnitude, reflecting a relative increase in charge compensation with δ. Figure 5e,f reveals that in LSF82, the compensation remains dominated by $[Fe^{\cdot}_{Fe}]$, whereas in LSF64, the proportion of charge compensated by oxygen vacancies increases significantly. This observation suggests that as the Sr content increases, the formation of excess $[Fe^{\cdot}_{Fe}]$ becomes energetically unfavorable, promoting δ formation to maintain. This behavior is consistent with theoretical predictions based on electronic structure analysis with Density Functional Theory (DFT) calculations [42, 95]. Specifically, Sr doping increases the covalency of Fe—O bonds and reduces charge localization on Fe ions. These changes weaken the Fe—O bonding interactions and lower the oxygen vacancy formation energy, thereby promoting δ formation over hole generation at higher Sr concentrations [95]. Furthermore, Das et al. have shown that the oxygen vacancy formation energy in $La_{1-x}Sr_xFeO_{3-\delta}$ significantly decreases (up to ~3 eV) with increasing Sr content, especially in the cubic and rhombohedral phases, further supporting the enhanced vacancy formation tendency in Sr-rich LSF composition [42]. As

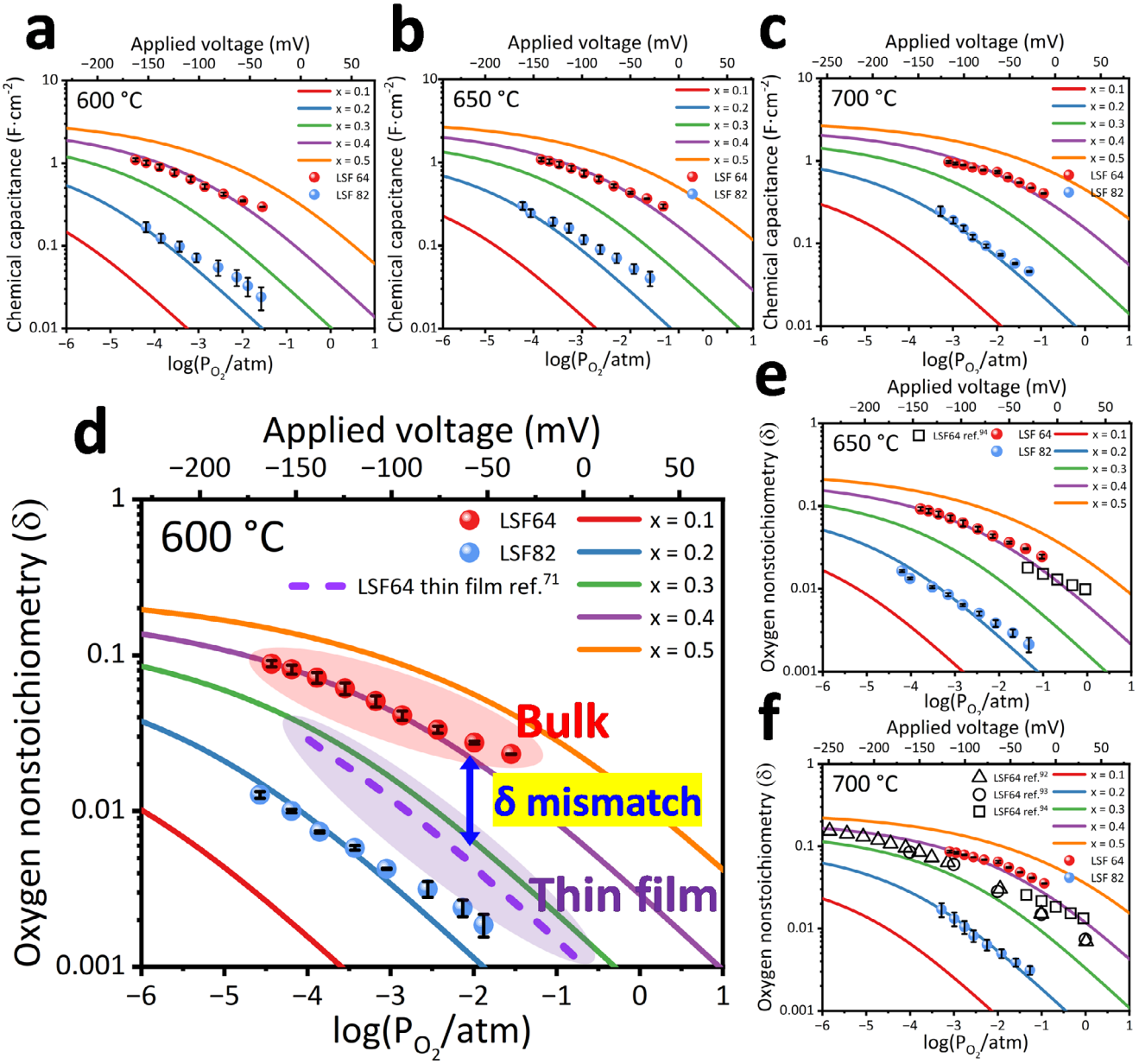

FIGURE 4 | Experimental and reference data of chemical capacitance and oxygen vacancy. Chemical capacitance at different Sr doping content as a function of applied voltage and equivalent oxygen partial pressure at a) 600°C, b) 650°C, and c) 700°C. Oxygen vacancy at different Sr doping content as a function of applied voltage and equivalent oxygen partial pressure at d) 600°C with reference thin film electrode [71], e) 650°C with reference TG data [92] and f) 700°C with reference TG data [92–94].

illustrated in Figure 3c, the dense bulk electrode system enables a comprehensive evaluation of both δ and $[Fe_{Fe}^{\cdot}]$ across various compositions under operating conditions via in situ impedance measurements.

2.3 | Degradation Analysis of Surface Exchange Coefficient and Chemical Capacitance

Understanding the degradation mechanisms of perovskite-based electrodes is critical for enhancing the long-term performance and durability of SOCs. Although various factors, such as increased polarization resistance, A-site Sr surface segregation, and microstructural coarsening, have been proposed to explain performance degradation, these insights have largely been derived from post-mortem analyses, offering limited understanding of the dynamic evolution of electrochemical properties under real operating conditions [96, 97]. A key challenge lies in the in situ monitoring of defect chemistry and surface reaction kinetics, hindered by the lack of robust methodologies for investigating charge carrier dynamics under realistic operating conditions.

The dense bulk electrode system used in this study offers a powerful platform to overcome these limitations. Owing to its well-defined geometry and suppressed microstructural artifacts, it enables direct, in situ analysis of both k and δ under realistic electrochemical environments. This approach allows for quantitative tracking of degradation phenomena via measurable

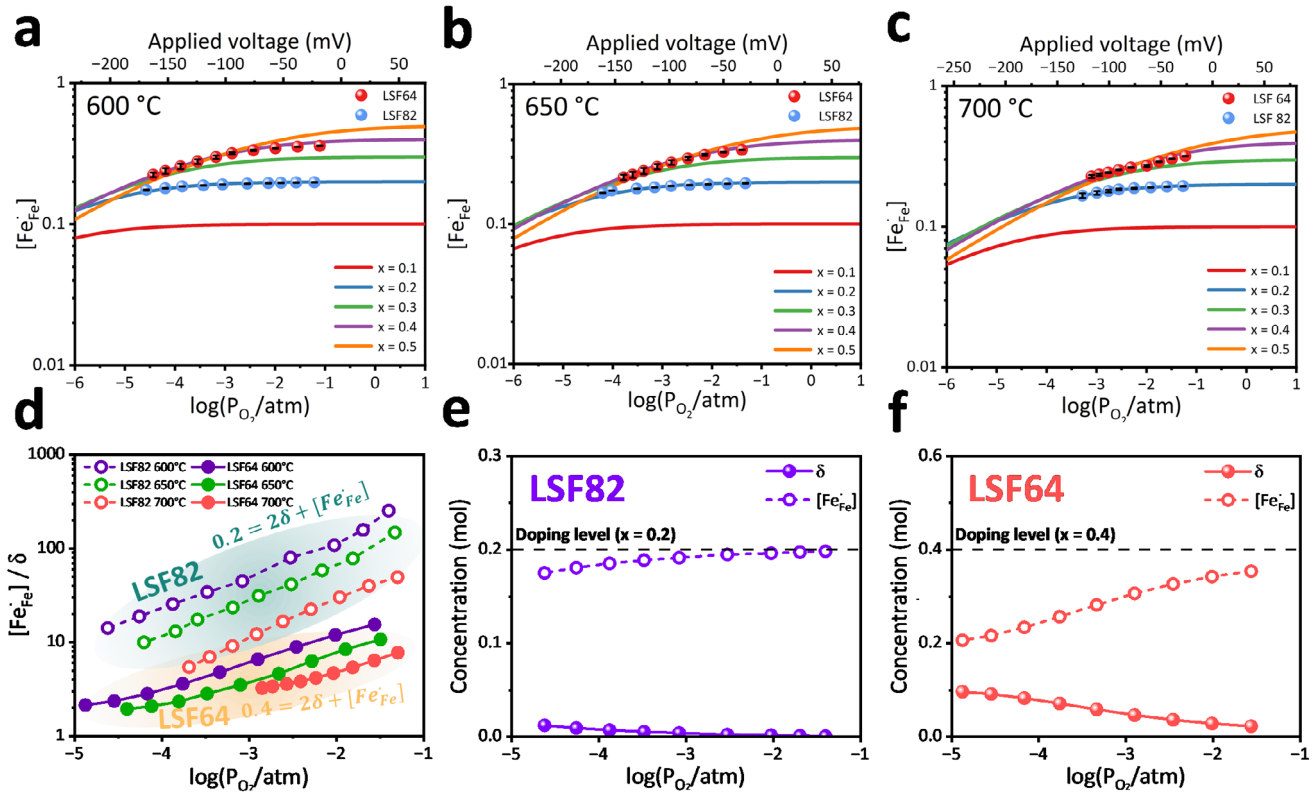

FIGURE 5 | Comparison of oxygen vacancy and hole concentration. $[Fe_{Fe}^{\cdot}]$ concentration at different Sr doping content as a function of applied voltage and equivalent oxygen partial pressure at a) 600°C, b) 650°C, and c) 700°C. d) Comparison of $[Fe_{Fe}^{\cdot}]/\delta$ ratio at $x = 0.2$ and $x = 0.4$. δ and $[Fe_{Fe}^{\cdot}]$ concentrations for e) LSF82 and f) LSF64.

changes in k and C_δ, providing new insights into the mechanisms governing electrode degradation. Building on the earlier evaluation of impedance-derived surface resistance, a more comprehensive understanding of the oxygen surface exchange behavior can be achieved by comparing different definitions of k. Specifically, k can be experimentally determined through three complementary approaches: the electrical surface exchange coefficient (k^q), tracer surface exchange coefficient (k^*) measured by SIMS, and chemical surface exchange coefficient (k_{chem}) extracted from ECR. These values reflect different aspects of the oxygen incorporation process depending on the measurement method and dominant charge carriers. For electron-rich MIEC materials, the relationship between these coefficients can be described as follows [98]:

$$k^q \approx k^* \approx \frac{k_{chem}}{\omega_O} \tag{7}$$

where $\omega_O (= \frac{c_O}{RT}\frac{\partial \mu_O}{\partial c_O})$ is the thermodynamic factor. Using Equation 7, k^* and k_{chem} can be inferred from k^q. Through this relationship, k_{chem} can be simply derived as $k_{chem} = \omega L$, where ω is the characteristic frequency in the Nyquist plot.

Figure 6a presents the Arrhenius plots of k^q obtained from the LSF64 dense bulk electrode, along with the k_{chem} values derived using the ω and L. For comparison, values derived from previous studies, based on thin film systems (k^q, k_{chem}) and bulk samples using transient analysis methods (k_{chem}) are included. In the dense bulk electrode system, the resistance associated with the oxygen exchange reaction is prominently observed in the impedance spectra. This pronounced surface exchange resistance enables straightforward extraction of k using Equation 1. The k^q values obtained from the dense bulk electrode system and k_{chem} values converted from k^q show good agreement with literature data. This consistency across multiple definitions and systems reinforces the validity and broader applicability of the dense bulk electrode platform for quantifying oxygen surface exchange kinetics under realistic operating conditions.

A key advantage of the dense bulk electrode system lies in its ability to enable in situ evaluation of k and δ simultaneously. Figure 6b illustrates the long-term degradation behavior of these two parameters under OCV conditions. The parameters were obtained by conducting in situ measurements of the time-dependent evolution of impedance spectra (Figure S8). Compared with conventional thin-film electrodes, the dense bulk system exhibits a significantly lower rate of surface degradation [81]. Notably, while C_δ remains stable over time, a substantial decline is observed in k^q. Because k^q is highly sensitive to surface-related processes, while C_δ predominantly reflects the bulk oxygen stoichiometry of LSF, the observed degradation in k^q is primarily attributable to the reduction in active surface sites, likely caused by localized phase decomposition or formation of surface precipitates. This interpretation is further supported by surface SEM analysis, which reveals the formation of precipitates as evidence of surface degradation (Figure S9). In contrast, the minimal change in C_δ, only a 2.5% reduction, suggests that the concentration of oxygen vacancies in the entire electrode

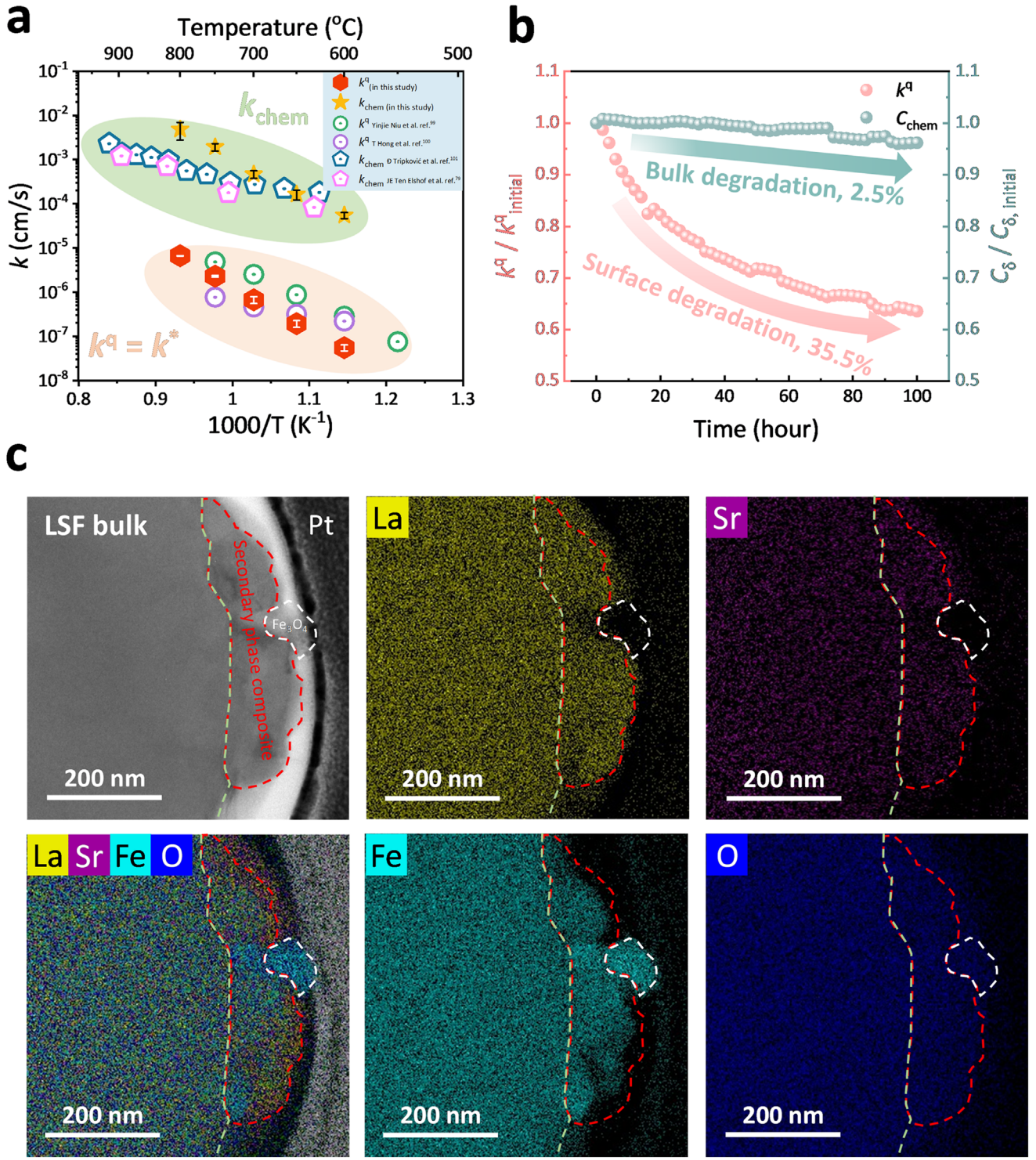

FIGURE 6 | Degradation of surface exchange coefficient and chemical capacitance at OCV conditions over 100 h. a) Surface exchange coefficients of LSF [79, 99–101]. b) Surface exchange coefficient and chemical capacitance degradation behavior of LSF64 electrode during 100 h at 700°C and OCV conditions. c) TEM-EDX mapping of the LSF surface of 100 h degraded sample under OCV condition.

decreased by only 2.5%. Assuming that this reduction is localized near the surface owing to structural degradation, it can be inferred that only a surface region corresponding to approximately 2.5% of the total electrode thickness experienced significant deterioration. Therefore, considering the total electrode thickness of ~8.9 μm, this reduction corresponds to oxygen depletion within a surface region estimated to be approximately 225 nm. To experimentally validate the predicted structural changes at the electrode surface associated with the reduction in δ, transmission electron microscopy with energy dispersive X-ray spectroscopy (TEM-EDX) was performed. Figure 6c shows the TEM-EDX results obtained from the surface of the LSF64 electrode after thermal aging at 700°C for 100 h under OCV conditions. The thickness of the degraded surface layer, approximately 200 nm, closely

matches the ~220 nm value predicted from the electrochemical reduction in C_δ, validating the accuracy of the spatial extent of degradation inferred from impedance analysis. In addition, EDX line profiles reveal the breakdown of the original LSF64 composition and emergence of a compositionally distinct secondary phase (Figure S10). This altered zone, characterized by changes in the relative atomic concentrations of La, Sr, Fe, and O, spans approximately 200 nm from the surface, further supporting the presence of a structurally and chemically modified layer consistent with the degradation depth estimated electrochemically. As shown in Figure S11, fast Fourier transform (FFT) pattern analysis further confirms the presence of a Fe-rich crystalline precipitate identified as α-Fe_2O_3 (with diffraction patterns corresponding to the (220) and (311) planes), as well as a dense surface layer composed of a La—Sr—Fe—O—based secondary phase. Overall, these findings strongly suggest that the formation of secondary phases at the electrode surface is closely linked to the observed suppression of oxygen exchange kinetics.

Although the present study focuses on a 100 h operational window, the observed degradation trends provide insight into the expected long-term behavior. As shown in Figure 6b, the degradation rate of k^q is pronounced at early times and progressively decreases, approaching a quasi-saturated regime by the end of the test. This behavior suggests a transition from an initially surface-driven process to a diffusion-limited regime at longer times. In contrast, C_δ remains nearly constant throughout the entire duration, indicating that the bulk defect chemistry is preserved. These results imply that degradation is primarily confined to the surface or near-surface region and is unlikely to propagate into the bulk lattice under the investigated operating conditions. Consequently, it is predicted that the bulk chemical capacitance will not undergo a substantial collapse even over extended operational timescales, as the thermodynamic robustness of the LSF lattice effectively confines the chemical and structural modifications to the narrow surface region. By simultaneously tracking the evolution of k and C_δ, this system provides a powerful platform for elucidating time-dependent degradation phenomena in MIEC electrodes with high spatial and mechanistic resolution. While previous studies have inferred performance loss from ex situ structural observations [11, 12, 72], our dense bulk platform enables direct correlation between electrochemical parameters and local compositional evolution. This provides a new analytic framework for evaluating surface aging in MIEC electrodes with high spatial and kinetic resolution. Thus, the proposed approach opens a path toward predictive monitoring of surface degradation under real operating conditions and offers a foundation for future design strategies targeting long-term electrode stability. Furthermore, while this study utilizes a dense bulk architecture to isolate intrinsic phenomena, the obtained k and δ values provide a useful framework for analyzing practical SOC electrodes with complex porous microstructures. While porous structures are primarily employed in practical devices to minimize electrode resistance through surface area maximization, our dense platform enables the direct evaluation of material-specific performance without microstructural interference. Since intrinsic surface kinetics are often obscured in porous architectures, our results serve as a comparative basis to distinguish between material-specific activity and microstructural effects. Moreover, the reported δ data acts as a reliable thermodynamic basis for assessing the chemical state and charge carrier concentration of porous electrodes. By providing these intrinsic parameters, our platform enables accurate performance prediction and mechanistic analysis, bridging the gap between model-scale investigations and the rational design of practical electrochemical devices.

3 | Conclusion

This study establishes a novel in situ characterization framework capable of simultaneously quantifying k and δ under realistic SOC operating conditions. By modulating oxygen chemical potential through the application of overpotentials, we successfully achieved a consistent assessment of both kinetic and thermodynamic parameters within a single experimental setup. Most importantly, this approach enabled us to track the dynamic evolution of electrode properties during long-term operation, providing deep insights into degradation mechanisms. We observed that while surface exchange kinetics deteriorated significantly due to surface-localized secondary phase formation and Sr segregation, the bulk oxygen vacancy concentration remained remarkably stable. This finding, corroborated by TEM-EDX analysis, confirms that the observed performance loss is primarily driven by surface-specific degradation rather than bulk thermodynamic instability. Consequently, this work provides a diagnostic framework bridging the gap between model studies and practical device environments, offering a pathway toward the rational design of durable electrochemical systems.

4 | Experimental Section

4.1 | Preparation of Powder and Dense Bulk Electrode through Tape Casting

In this study, $La_{1-x}Sr_xFeO_{3-\delta}$ (LSF), a representative perovskite material with sufficient electronic and ionic conductivities and stable performance, was used as the electrode material. $Gd_{0.1}Ce_{0.9}O_{1.95}$ (GDC) (Korea, K-ceracell), which exhibits excellent oxygen ion conductivity, was used as the electrolyte. The $La_{0.6}Sr_{0.4}FeO_{3-\delta}$ (LSF64) powder was manufactured by the solid-state reaction method using La_2O_3 (Japan, Kojundo Chemical Laboratory), $SrCO_3$ (Korea, Daejung), and Fe_2O_3 (USA, Aldrich) according to the target composition. The synthesized LSF64 was calcined at 1000°C for 10 h. The X-ray diffraction (XRD) pattern of the LSF64 powder was consistent with reported patterns of LSF64 (Figure S1). $La_{0.8}Sr_{0.2}FeO_{3-\delta}$ (LSF82) (Korea, K-ceracell) powder, belonging to the same LSF material system but with a different Sr composition, was used as a reference material.

To prepare a slurry, ethanol was used as a solvent and mixed with a dispersant, plasticizer, and binder, followed by ball milling with zirconia balls. Ball milling was performed for 48 h. Afterwards, the slurry was applied on a polyethylene film to obtain a green tape with a thickness of approximately 9 μm. To lower the sintering temperature of the electrolyte to match that of LSF (1350°C), 1 vol.% of $La_{0.6}Sr_{0.4}Co_{0.2}Fe_{0.8}O_{3-\delta}$ (LSCF, Korea, K-ceracell) was added to GDC as a sintering aid.

For the electrolyte, a green sheet was produced in the same manner as the electrode, yielding a green tape with a thickness of approximately 20 μm. The electrolyte was laminated using warm

isostatic pressure (WIP) to attain a thickness of approximately 600 μm. The electrode and electrolyte were cut using a laser cutting machine, and then the electrode and electrolyte were stacked under a pressure of 43 MPa and 70°C using WIP. Then, the manufactured specimen was sintered at 1350°C for 6 h to confirm its dense structure. To prepare the porous LSCF paste as the counter electrode, LSCF powder and organic solution (Heraeus V-006, Germany, Heraeus) were mixed in a specific ratio and manufactured through a 3-roll milling process.

The counter electrode was fabricated by coating the porous LSCF paste on the opposite side of the dense electrode using the brush-painting method, followed by heat treatment at 1000°C for 3 h. To evaluate the electrochemical properties, Pt paste (Germany, Heraeus) was brushed, and Pt mesh was attached to both the dense and porous electrodes, followed by calcination at 800°C for 1 h.

4.2 | Characterization

Phase analysis was performed on synthesized LSF64 powder and dense LSF64 bulk electrode using an X-ray diffractometer (XRD, Rigaku Corporation, SmartLab, Japan) with Cu Kα source. Electrochemical analysis was performed through impedance measurement (EIS, Bio-Logic, SP-240, France) with a frequency range of 1 MHz to 5 mHz and an AC voltage of 10 mV and 6 points per decade. In addition, the microstructure of the interface and surface of the bulk electrode manufactured by co-sintering was analyzed using a scanning electron microscope (SEM, Thermo Fisher Scientific, Verios 5 UC, America). The transmission electron microscopy (TEM) samples were prepared using a dual-beam focused ion beam (FIB, Thermo Fisher Scientific, Helios Nano Lab 450, USA) method. Elemental mapping analysis for the electrode surface was performed using transmission electron microscopy energy dispersive X-ray spectroscopy (TEM-EDX, FEI Company, Tecnai G^2 F30 S-Twin, USA) in the scanning transmission electron microscopy (STEM) imaging mode. A fast Fourier transform (FFT) analysis of the TEM image was performed using Gatan Digital Micrograph software.

Author Contributions

T.K. performed the majority of the experiments, analyzed the data, and wrote the manuscript. J.L. conducted selected experiments and analyzed the results. H.J.P. and J.H.Y. contributed to interpreting the experimental results and data analysis. J.M.S. provided critical input, analyzed the data, and revised the manuscript. J.H.J. conceived and supervised the study and wrote the manuscript. All authors discussed the results and commented on the paper.

Acknowledgements

This work was supported by the Technology Innovation Program (or Industrial Strategic Technology Development Program-Material and Component Technology Development (R&D)) (RS-2024-00432125, Development of Evaluation and Electrochemical Diagnostics Technology for Advanced K-SOEC Stack) funded by the Ministry of Trade, Industry & Energy (MOTIE, Korea). This work was also supported by the National Research Foundation (NRF) of Korea, funded by the Government of Korea (MSIT) (Research project number: RS-2023-00236572). This research was also supported by the H2GATHER through the National Research Foundation of Korea (NRF) funded by the Ministry of Science and ICT (RS-2025-02314320).

Conflicts of Interest

The authors declare no conflicts of interest.

Data Availability Statement

The data that support the findings of this study are included in the published article and its supplemental information. Additional data can be available from the lead contact upon reasonable request.

References

1. A. Hauch, R. Küngas, P. Blennow, et al., "Recent Advances in Solid Oxide Cell Technology for Electrolysis," *Science* 370 (2020): aba6118.

2. M. Ni, M. K. Leung, and D. Y. Leung, "Technological Development of Hydrogen Production by Solid Oxide Electrolyzer Cell (SOEC)," *International Journal of Hydrogen Energy* 33 (2008): 2337–2354.

3. C. Duan, R. Kee, H. Zhu, et al., "Highly Efficient Reversible Protonic Ceramic Electrochemical Cells for Power Generation and Fuel Production," *Nature Energy* 4 (2019): 230–240.

4. J. T. Irvine, D. Neagu, M. C. Verbraeken, C. Chatzichristodoulou, C. Graves, and M. B. Mogensen, "Evolution of the Electrochemical Interface in High-Temperature Fuel Cells and Electrolysers," *Nature Energy* 1 (2016): 15014.

5. M. Dokiya, "SOFC System and Technology," *Solid State Ionics* 152 (2002): 383–392.

6. F. Hu, B. He, K. Chen, et al., "Single-Atom Anchored on Perovskite With Strong Metal-Oxide Interaction for Efficient High Temperature CO_2 Electrolysis," *Advanced Materials* 38 (2025): 12310.

7. Z. Chen, L. Zhang, S. Sun, and G. Zhang, "Electrochemical Cell Designs for Efficient Carbon Dioxide Reduction and Water Electrolysis: Status and Perspectives," *Advanced Materials* 37 (2025): 2505287.

8. H. Zhang, K. Xu, F. He, et al., "Challenges and Advancements in the Electrochemical Utilization of Ammonia Using Solid Oxide Fuel Cells," *Advanced Materials* 36 (2024): 2313966.

9. M. Yang, S. Liu, X. Shen, et al., "Robust Cathode for Efficient CO_2 Electrolysis Driven by Entropy Engineering in Solid Oxide Electrolysis Cells," *ACS Energy Letters* 9 (2024): 3818–3827.

10. J. Lee, Y. Shin, T. Kim, et al., "Phase Stability of Perovskite Oxide Electrodes Under Operating Condition in Solid Oxide Fuel Cell," *Chemistry of Materials* 36 (2024): 2933–2943.

11. Y. Yan, Q. Fang, L. Blum, and W. Lehnert, "Performance and Degradation of an SOEC Stack With Different Cell Components," *Electrochimica Acta* 258 (2017): 1254–1261.

12. F. Tietz, D. Sebold, A. Brisse, and J. Schefold, "Degradation Phenomena in a Solid Oxide Electrolysis Cell After 9000 h of Operation," *Journal of Power Sources* 223 (2013): 129–135.

13. H. Choi, J. Shin, C. Yeon, et al., "Unveiling the High-Temperature Degradation Mechanism of Solid Oxide Electrolysis Cells Through Direct Imaging of Nanoscale Interfacial Phenomena," *Energy & Environmental Science* 17 (2024): 5410–5420.

14. S. K. Kim, H. J. Lee, J. Y. Moon, et al., "Understanding the Phase Stability of Yttria Stabilized Zirconia Electrolyte Under Solid Oxide Electrolysis Cell Operation Conditions," *Journal of Materials Chemistry A* 12 (2024): 8319–8330.

15. T. Yang, Y. Fan, J. Liu, et al., "Multiphysics Modeling of SOFC Performance Degradation Caused by Interface Delamination and Active Layer Cracking," *International Journal of Hydrogen Energy* 47 (2022): 41124–41137.

16. J. Lee, Z. Ma, T. Kim, et al., "Real-Time Analysis of Solid Oxide Electrolysis Cells Manufactured by Ceramic Sintering Process via Operando

TEM and Electrochemical Impedance Spectroscopy," *Small* 21 (2025): 04862.

17. J. Lee, J. Park, T. Kim, et al., "Mechanistic Insights Into Performance and Stability Enhancement of Infiltrated Solid Oxide Electrochemical Cell Electrodes," *Small* 21 (2025): 06595.

18. H. G. Seo, A. Staerz, D. S. Kim, J. M. Lebeau, and H. L. Tuller, "Tuning Surface Acidity of Mixed Conducting Electrodes: Recovery of Si-Induced Degradation of Oxygen Exchange Rate and Area Specific Resistance," *Advanced Materials* 35 (2023): 2208182.

19. F. Giannici, G. Canu, A. Chiara, et al., "Cation Diffusion and Segregation at the Interface Between Samarium-Doped Ceria and LSCF or LSFCu Cathodes Investigated With X-ray Microspectroscopy," *ACS Applied Materials & Interfaces* 9 (2017): 44466–44477.

20. A. V. Virkar, "A model for solid oxide fuel cell (SOFC) stack degradation," *Journal of Power Sources* 172 (2007): 713–724.

21. B.-K. Park, Q. Zhang, P. W. Voorhees, and S. A. Barnett, "Conditions for Stable Operation of Solid Oxide Electrolysis Cells: Oxygen Electrode Effects," *Energy & Environmental Science* 12 (2019): 3053–3062.

22. C. Ni, J. Zhou, Z. Zhang, S. Li, J. Ni, K. Wu, and J. T. Irvine, "Iron-Based Electrode Materials for Solid Oxide Fuel Cells and Electrolysers," *Energy & Environmental Science* 14 (2021): 6287–6319.

23. J. Lee, T. Kim, H. J. Lee, et al., "Understanding the Degradation Mechanisms of Ba-Based Double Perovskite Electrodes for Solid Oxide Electrochemical Cells," *Chemical Engineering Journal* 505 (2025): 159654.

24. M. Maide, K. Lillmaa, L. K. Salvan, et al., "Influence of Electrolyte Scaffold Microstructure and Loading of MIEC Material on the Electrochemical Performance of RSOC Fuel Electrode," *Fuel Cells* 18 (2018): 789–799.

25. Y. Chen, Y. Fan, H. W. Abernathy, and X. Song, "Internal Surface and Grain Boundary Degradation of $La_{0.6}Sr_{0.4}Co_{0.2}Fe_{0.8}O_{3-\delta}/Sm_{0.2}Ce_{0.8}O_{2-\delta}$ Porous Air Electrode of Solid Oxide Fuel Cells Operated in Humidified Air," *ACS Applied Energy Materials* 8 (2025): 15348–15356.

26. A. He, J. Onishi, J. Gong, and N. Shikazono, "Microstructure Optimization of Porous Mixed Ionic and electronic Conducting Cathode for Solid Oxide Fuel Cells," *Journal of Power Sources* 478 (2020): 228771.

27. N. Kim, N. H. Perry, and E. Ertekin, "Atomic Modeling and Electronic Structure of Mixed Ionic–Electronic Conductor $SrTi_{1-x}Fe_xO_{3-x/2+\delta}$ Considered as a Mixture of $SrTiO_3$ and $Sr_2Fe_2O_5$," *Chemistry of Materials* 31 (2018): 233–243.

28. M. A. Laguna-Bercero, J. A. Kilner, and S. J. Skinner, "Performance and Characterization of (La, Sr)MnO_3 /YSZ and $La_{0.6}$ $Sr_{0.4}$ $Co_{0.2}$ $Fe_{0.8}$ O_3 Electrodes for Solid Oxide Electrolysis Cells," *Chemistry of Materials* 22 (2010): 1134–1141.

29. A. Yan, M. Cheng, Y. Dong, W. Yang, V. Maragou, S. Song, and P. Tsiakaras, "Investigation of a $Ba_{0.5}Sr_{0.5}Co_{0.8}Fe_{0.2}O_{3-\delta}$based cathode IT-SOFC," *Applied Catalysis B: Environmental* 66 (2006): 64–71.

30. G. D. Han, K. Bae, E. H. Kang, H. J. Choi, and J. H. Shim, "Inkjet Printing for Manufacturing Solid Oxide Fuel Cells," *ACS Energy Letters* 5 (2020): 1586–1592.

31. D. Rembelski, J.-P. Viricelle, L. Combemale, and M. Rieu, "Characterization and Comparison of Different Cathode Materials for SC-SOFC: LSM, BSCF, SSC, and LSCF," *Fuel Cells* 12 (2012): 256–264.

32. D. Ding, M. Liu, Z. Liu, X. Li, K. Blinn, X. Zhu, and M. Liu, "Efficient Electro-Catalysts for Enhancing Surface Activity and Stability of SOFC Cathodes," *Advanced Energy Materials* 3 (2013): 1149–1154.

33. S. J. Kim and G. M. Choi, "Stability of LSCF electrode With GDC Interlayer in YSZ-Based Solid Oxide Electrolysis cell," *Solid State Ionics* 262 (2014): 303–306.

34. K. Murata, T. Fukui, H. Abe, M. Naito, and K. Nogi, "Morphology Control of La(Sr)Fe$(Co)_{O3-a}$ Cathodes for IT-SOFCs," *Journal of Power Sources* 145 (2005): 257–261.

35. N. Tsvetkov, Q. Lu, L. Sun, E. J. Crumlin, and B. Yildiz, "Improved Chemical and Electrochemical Stability of Perovskite Oxides With Less Reducible Cations at the Surface," *Nature Materials* 15 (2016): 1010–1016.

36. Y. Chen, Y. Choi, S. Yoo, et al., "A Highly Efficient Multi-phase Catalyst Dramatically Enhances the Rate of Oxygen Reduction," *Joule* 2 (2018): 938–949.

37. A. J. Majewski, A. Khodimchuk, D. Zakharov, et al., "Oxygen Surface Exchange Properties and Electrochemical Activity of Lanthanum Nickelates," *Journal of Solid State Chemistry* 312 (2022): 123228.

38. N. Lyskov, M. Kaluzhskikh, L. Leonova, G. Mazo, S. Y. Istomin, and E. Antipov, "Electrochemical Characterization of Pr_2CuO_4 Cathode for IT-SOFC," *International Journal of Hydrogen Energy* 37 (2012): 18357–18364.

39. M. Z. Ahmad, S. H. Ahmad, R. S. Chen, A. F. Ismail, R. Hazan, and N. A. Baharuddin, "Review on Recent Advancement in Cathode Material for Lower and intermediate temperature solid oxide fuel cells application," *International Journal of Hydrogen Energy* 47 (2022): 1103–1120.

40. G. Cohn and E. D. Wachsman, "In-Operando Determination of SOFC Cathode Oxygen Surface Exchange Coefficients for Enhanced Oxygen Reduction Reaction Kinetics," *Journal of The Electrochemical Society* 164 (2017): F3035–F3044.

41. H. Cai, C. Xia, X. Wang, W. Dong, et al., "Diverse Functions of Oxygen Vacancies for Oxygen Ion Conduction," *ACS Applied Energy Materials* 5 (2022): 11122–11132.

42. T. Das, J. D. Nicholas, and Y. Qi, "Composition, Crystallography, and Oxygen Vacancy Ordering Impacts on the Oxygen ion Conductivity of Lanthanum Strontium Ferrite," *Physical Chemistry Chemical Physics* 22 (2020): 9723–9733.

43. P. Haworth, S. Smart, J. Serra, and J. D. Da Costa, "Combined Investigation of Bulk Diffusion and Surface Exchange Parameters of Silver Catalyst Coated Yttrium-Doped BSCF membranes," *Physical Chemistry Chemical Physics* 14 (2012): 9104.

44. P.-M. Geffroy, L. Guironnet, H. J. Bouwmeester, T. Chartier, J.-C. Grenier, and J.-M. Bassat, "Influence of Oxygen Partial Pressure on the Oxygen Diffusion and Surface Exchange Coefficients in Mixed Conductors," *Journal of the European Ceramic Society* 39 (2019): 59–65.

45. V. Metlenko, W. Jung, S. R. Bishop, H. L. Tuller, and R. A. De Souza, "Oxygen Diffusion and Surface Exchange in the Mixed Conducting Oxides $SrTi_{1-y}Fe_yO_{3-\delta}$," *Physical Chemistry Chemical Physics* 18 (2016): 29495–29505.

46. Y. Cao, M. J. Gadre, A. T. Ngo, S. B. Adler, and D. D. Morgan, "Factors Controlling Surface Oxygen Exchange in Oxides," *Nature Communications* 10 (2019): 1346.

47. Y. Wang, L. Zhang, and C. Xia, "Enhancing Oxygen Surface Exchange Coefficients of Strontium-Doped Lanthanum Manganates With Electrolytes," *International Journal of Hydrogen Energy* 37 (2012): 2182–2186.

48. A. Berenov, A. Atkinson, J. Kilner, E. Bucher, and W. Sitte, "Oxygen Tracer Diffusion and Surface Exchange Kinetics in $La_{0.6}Sr_{0.4}CoO_{3-\delta}$," *Solid State Ionics* 181 (2010): 819–826.

49. M. Kuhn, S. Hashimoto, K. Sato, K. Yashiro, and J. Mizusaki, "Oxygen Nonstoichiometry and Thermo-Chemical Stability of $La_{0.6}Sr_{0.4}CoO_{3-\delta}$," *Journal of Solid State Chemistry* 197 (2013): 38–45.

50. J. Mizusaki, Y. Mima, S. Yamauchi, K. Fueki, and H. Tagawa, "Nonstoichiometry of the Perovskite-Type Oxides $La_{1-x}Sr_xCoO_{3-\delta}$," *Journal of Solid State Chemistry* 80 (1989): 102–111.

51. J. Mizusaki, M. Yoshihiro, S. Yamauchi, and K. Fueki, "Nonstoichiometry and Defect Structure of the Perovskite-Type oxides $La_{1-x}Sr_xFeO_{3-\delta}$," *Journal of Solid State Chemistry* 58 (1985): 257–266.

52. V. Cherepanov, T. Aksenova, E. Kiselev, and L. Gavrilova, "Oxygen Nonstoichiometry and Defect Structure of Perovskite-Type Oxides in the La–Sr–Co–(Fe, Ni)–O systems," *Solid State Sciences* 10 (2008): 438–443.

53. M. Lankhorst and H. Bouwmeester, "Determination of Oxygen Nonstoichiometry and Diffusivity in Mixed Conducting Oxides by Oxygen Coulometric Titration: II. Oxygen Nonstoichiometry and Defect Model for," *Journal of The Electrochemical Society* 144 (1997): 1268–1273.

54. J. Yoo, C. Y. Yoo, J. H. Yu, and A. J. Jacobson, "Determination of Oxygen Nonstoichiometry in $SrFeO_{3-\delta}$ by Solid-State Coulometric Titration," *Journal of the American Ceramic Society* 100 (2017): 2690–2699.

55. W. Araki, Q. Miaolong, and Y. Arai, "Oxygen non-stoichiometry of $La_{0.6}Sr_{0.4}Co_{0.2}Fe_{0.8}O_{3-\delta}$ Under Uniaxial Compression Evaluated by Coulometric Titration," *Electrochimica Acta* 253 (2017): 339–343.

56. S. Sengodan, Y.-W. Ju, O. Kwon, et al., "Self-Decorated MnO Nanoparticles on Double Perovskite Solid Oxide Fuel Cell Anode by in Situ Exsolution," *ACS Sustainable Chemistry & Engineering* 5 (2017): 9207–9213.

57. D. Chen and Z. Shao, "Surface Exchange and Bulk Diffusion Properties of $Ba_{0.5}Sr_{0.5}Co_{0.8}Fe_{0.2}O_{3-\delta}$ Mixed Conductor," *International Journal of Hydrogen Energy* 36 (2011): 6948–6956.

58. D.-K. Lim, S.-Y. Jeon, B. Singh, J.-Y. Park, and S.-J. Song, "Surface Exchange Kinetics and Chemical Diffusivities of $BaZr_{0.2}Ce_{0.65}Y_{0.15}O_{3-\delta}$ by Electrical Conductivity Relaxation," *Journal of Alloys and Compounds* 610 (2014): 301–307.

59. D. Kim, J. W. Park, B.-H. Yun, J. H. Park, and K. T. Lee, "Correlation of Time-Dependent Oxygen Surface Exchange Kinetics With Surface Chemistry of $La_{0.6}$ $Sr_{0.4}Co_{0.2}Fe_{0.8}O_{3-\delta}$ Catalysts," *ACS Applied Materials & Interfaces* 11 (2019): 31786–31792.

60. L. Zhang, S. Wang, H. Huang, Y. Li, Y. Lu, and C. Xia, "Promotion Effect of Metal Nanoparticle on Surface Exchange Reaction of (La,Sr)MnO_3 Film With Different Orientation," *Journal of The Electrochemical Society* 164 (2017): F610–F615.

61. B. Hu, Y. Wang, Z. Zhu, C. Xia, and H. J. Bouwmeester, "Measuring oxygen Surface Exchange Kinetics on Mixed-Conducting Composites by Electrical conductivity relaxation," *Journal of Materials Chemistry A* 3 (2015): 10296–10302.

62. R. Chater, S. Carter, J. Kilner, and B. Steele, "Development of a Novel SIMS Technique for Oxygen Self-Diffusion and Surface Exchange Coefficient Measurements in Oxides of High Diffusivity," *Solid State Ionics* 53-56 (1992): 859–867.

63. M. Kamiya, E. Shimada, Y. Ikuma, M. Komatsu, and H. Haneda, "Intrinsic and Extrinsic Oxygen Diffusion and Surface Exchange Reaction in Cerium Oxide," *Journal of The Electrochemical Society* 147 (2000): 1222.

64. J. A. Kilner, S. J. Skinner, and H. H. Brongersma, "The Isotope Exchange Depth Profiling (IEDP) Technique Using SIMS and LEIS," *Journal of Solid State Electrochemistry* 15 (2011): 861–876.

65. W. Jung and H. L. Tuller, "Investigation of Cathode Behavior and Surface Chemistry of Model Thin Film $SrTi_{1-x}Fe_xO_{3-\delta}$ Electrode," *ECS Transactions* 25 (2009): 2775–2782.

66. D. Chen, S. R. Bishop, and H. L. Tuller, "Praseodymium-Cerium Oxide Thin Film Cathodes: Study of Oxygen Reduction Reaction Kinetics," *Journal of Electroceramics* 28 (2012): 62–69.

67. D. Lee, Y.-L. Lee, A. Grimaud, et al., "Enhanced Oxygen Surface Exchange Kinetics and Stability on Epitaxial $La_{0.8}Sr_{0.2}CoO_{3-\delta}$ Thin Films by $La_{0.8}Sr_{0.2}MnO_{3-\delta}$ Decoration," *The Journal of Physical Chemistry C* 118 (2014): 14326–14334.

68. L. Wang, R. Merkle, and J. Maier, "Oxygen Reduction Kinetics and Transport Properties of (Ba,Sr)(Co,Fe)$O_{3-\delta}$ and Related SOFC Cathode Materials," *ECS Transactions* 25 (2009): 2497–2505.

69. J. Fleig, H. R. Kim, J. Jamnik, and J. Maier, "Oxygen Reduction Kinetics of Lanthanum Manganite (LSM) Model Cathodes: Partial Pressure Dependence and Rate-Limiting Steps," *Fuel Cells* 8 (2008): 330–337.

70. T. Kawada, J. Suzuki, M. Sase, et al., "Determination of Oxygen Vacancy Concentration in a Thin Film of $La_{0.6}Sr_{0.4}CoO_{3-\delta}$ by an Electrochemical Method," *Journal of The Electrochemical Society* 149 (2002): E252.

71. D. Oi, N. Miyashita, R. A. Budiman, et al., "Elucidating Factors Governing the Discrepancy of Oxygen Vacancy Concentration Between $La_{0.6}Sr_{0.4}Co_{1-y}Fe_yO_{3-\delta}$ (y = 0, 0.2, 0.4, 0.6, 0.8, 1) Dense Film and Bulk Electrodes," *Journal of The Electrochemical Society* 172 (2025): 024506.

72. S. P. Simner, J. P. Shelton, M. D. Anderson, and J. W. Stevenson, "Interaction Between La(Sr)FeO_3 SOFC Cathode and YSZ Electrolyte," *Solid State Ionics* 161 (2003): 11–18.

73. M. D. Anderson, J. W. Stevenson, and S. P. Simner, "Reactivity of Lanthanide Ferrite SOFC Cathodes With YSZ Electrolyte," *Journal of Power Sources* 129 (2004): 188–192.

74. S. Sun and Z. Cheng, "Effects of H_2O and CO_2 on Electrochemical Behaviors of BSCF Cathode for Proton Conducting IT-SOFC," *Journal of The Electrochemical Society* 164 (2016): F81–F88.

75. G. Yang, W. Jung, S.-J. Ahn, and D. Lee, "Controlling the Oxygen Electrocatalysis on Perovskite and Layered Oxide Thin Films for Solid Oxide Fuel Cell Cathodes," *Applied Sciences* 9 (2019): 1030.

76. Z. Guan, D. Chen, and W. C. Chueh, "Analyzing the Dependence of Oxygen Incorporation Current Density on Overpotential and Oxygen Partial Pressure in Mixed Conducting Oxide Electrodes," *Physical Chemistry Chemical Physics* 19 (2017): 23414–23424.

77. S. Ovtar, M. Søgaard, K. Norrman, and P. V. Hendriksen, "Oxygen Exchange and Transport in $(La_{0.6}Sr_{0.4})_{0.98}FeO_{3-\delta}$—$Ce_{0.9}Gd_{0.1}O_{1.95}$ Dual-Phase Composites," *Journal of The Electrochemical Society* 165 (2018): F220–F231.

78. D. Sikstrom and V. Thangadurai, "A Tutorial Review on Solid Oxide Fuel Cells: Fundamentals, Materials, and Applications," *Ionics* 32 (2024): 5–30.

79. J. E. Ten Elshof, M. Lankhorst, and H. Bouwmeester, "Oxygen Exchange and Diffusion Coefficients of Strontium-Doped Lanthanum Ferrites by Electrical Conductivity Relaxation," *Journal of The Electrochemical Society* 144 (1997): 1060–1067.

80. E. N. Armstrong, K. L. Duncan, and E. D. Wachsman, "Effect of A and B-Site Cations on Surface Exchange Coefficient for ABO_3 Perovskite Materials," *Physical Chemistry Chemical Physics* 15 (2013): 2298–2308.

81. J. Lee, M. Kim, Y. Lee, and J. H. Joo, "Strategy to Elucidate the Reaction Mechanism of Electrodes for Realistic Solid Oxide Electrochemical Cells Using a Dense Bulk Material," *Chemistry of Materials* 33 (2021): 6290–6298.

82. H. Sumi, S. Takahashi, Y. Yamaguchi, and H. Shimada, "Lanthanum-Doped Ceria Interlayer Between Electrolyte and Cathode for Solid Oxide Fuel Cells," *Journal of Asian Ceramic Societies* 9 (2021): 609–616.

83. G. Yang, M. El Loubani, H. R. Chalaki, et al., "Tuning Ionic Conductivity in Fluorite Gd-Doped CeO_2 -Bixbyite RE_2O_3 (RE = Y and Sm) Multilayer Thin Films by Controlling Interfacial Strain," *ACS Applied Electronic Materials* 5 (2023): 4556–4563.

84. C. Riedl, M. U. Siebenhofer, A. Nenning, et al., "Surface Decorations on Mixed Ionic and Electronic Conductors: Effects on Surface Potential, Defects, and the Oxygen Exchange Kinetics," *ACS Applied Materials & Interfaces* 15 (2023): 26787–26798.

85. C. Riedl, A. Schmid, A. Nenning, et al., "Outstanding Oxygen Reduction Kinetics of $La_{0.6}Sr_{0.4}FeO_{3-\delta}$ Surfaces Decorated With Platinum Nanoparticles," *Journal of The Electrochemical Society* 167 (2020): 104514.

86. F. S. Baumann, "Electrode Kinetics of SOFC Cathodes: Thin Film Model Electrodes and Impedance Spectroscopy," Ph.D Thesis, University of Stuttgart, 2006.

87. A. Dutta, A. Kumar, and R. N. Basu, "Enhanced Electrical Conductivity in $Ce_{0.79}Gd_{0.20}Co_{0.01}O_{2-\delta}$ for Low Temperature Solid Oxide Fuel Cell Applications," *Electrochemistry Communications* 11 (2009): 699–701.

88. F. S. Baumann, J. Fleig, H.-U. Habermeier, and J. Maier, "$Ba_{0.5}Sr_{0.5}Co_{0.8}Fe_{0.2}O_{3-\delta}$ Thin Film Microelectrodes Investigated by Impedance Spectroscopy," *Solid State Ionics* 177 (2006): 3187–3191.

89. J. Fleig, F. S. Baumann, V. Brichzin, et al., "Thin Film Microelectrodes in SOFC Electrode Research," *Fuel Cells* 6 (2006): 284–292.

90. E. Mutoro, E. J. Crumlin, M. D. Biegalski, H. M. Christen, and Y. Shao-Horn, "Enhanced Oxygen Reduction Activity on Surface-Decorated Perovskite Thin Films for Solid Oxide Fuel Cells," *Energy & Environmental Science* 4 (2011): 3689–3696.

91. A. Schmid, G. M. Rupp, and J. Fleig, "Voltage and Partial Pressure Dependent Defect Chemistry in (La,Sr)$FeO_{3-\delta}$ Thin Films Investigated by Chemical Capacitance Measurements," *Physical Chemistry Chemical Physics* 20 (2018): 12016–12026.

92. M. Kuhn, S. Hashimoto, K. Sato, K. Yashiro, and J. Mizusaki, "Oxygen Nonstoichiometry, Thermo-Chemical Stability and Lattice Expansion of $La_{0.6}Sr_{0.4}FeO_{3-\delta}$," *Solid State Ionics* 195 (2011): 7–15.

93. M. Kuhn, Y. Fukuda, S. Hashimoto, K. Sato, K. Yashiro, and J. Mizusaki, "Oxygen Nonstoichiometry of Perovskite-type $La_{0.6}Sr_{0.4}Co_{1-y}Fe_yO_{3-\delta}$ (y=0, 0.2, 0.4, 0.5, 0.6, 0.8, 1) SOFC Cathode Materials," *ECS Transactions* 35 (2011): 1881–1890.

94. J. Song, D. Ning, and H. J. Bouwmeester, "Influence of Alkaline-Earth Metal Substitution on Structure, Electrical Conductivity and Oxygen Transport Properties of Perovskite-Type Oxides $La_{0.6}$ $A_{0.4}FeO_{3-\delta}$ (A = Ca, Sr and Ba)," *Physical Chemistry Chemical Physics* 22 (2020): 11984–11995.

95. Y. Feng, H. Jin, and S. Wang, "Oxygen Migration Performance of $LaFeO_3$ Perovskite-Type Oxygen Carriers With Sr Doping," *Physical Chemistry Chemical Physics* 25 (2023): 9216–9224.

96. S. Koohfar, M. Ghasemi, T. Hafen, et al., "Improvement of Oxygen Reduction Activity and Stability on a Perovskite Oxide Surface by Electrochemical Potential," *Nature Communications* 14 (2023): 7203.

97. B. Koo, K. Kim, J. K. Kim, H. Kwon, J. W. Han, and W. Jung, "Sr Segregation in Perovskite Oxides: Why It Happens and How It Exists," *Joule* 2 (2018): 1476–1499.

98. J. Maier, "Interaction of oxygen With Oxides: How to Interpret Measured Effective Rate Constants?," *Solid State Ionics* 135 (2000): 575–588.

99. Y. Niu, J. Sunarso, F. Liang, W. Zhou, Z. Zhu, and Z. Shao, "A Comparative Study of Oxygen Reduction Reaction on Bi- and La-Doped $SrFeO_{3-\delta}$ Perovskite Cathodes," *Journal of the Electrochemical Society* 158 (2010): B132–B138.

100. T. Hong, M. Y. Zhao, K. Brinkman, F. L. Chen, and C. R. Xia, "Enhanced Oxygen Reduction Activity on Ruddlesden–Popper Phase Decorated $La_{0.8}Sr_{0.2}FeO_{3-\delta}$ 3D Heterostructured Cathode for Solid Oxide Fuel Cells," *ACS Applied Materials & Interfaces* 9 (2017): 8659–8668.

101. Đ. Tripković, R. Küngas, M. B. Mogensen, and P. V. Hendriksen, "Surface Recrystallization—An Underestimated Phenomenon Affecting Oxygen Exchange Activity," *Journal of Materials Chemistry A* 7 (2019): 11782–11791.

Supporting Information

Additional supporting information can be found online in the Supporting Information section.

Supporting File: aenm70758-sup-0001-SuppMat.docx.